Construction and Building Materials 519 (2026) 145910

Contents lists available at ScienceDirect

Construction and Building Materials

journal homepage: www.elsevier.com/locate/conbuildmat

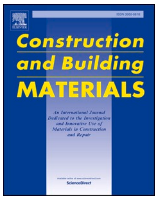

Integrity assessment of masonry dams using ground penetrating radar-based time-energy density approach

K. Panjami [a,b], P. Anbazhagan [a,*]

[a] *Department of Civil Engineering, Indian Institute of Science, Bangalore, Karnataka, India*
[b] *Department of Civil Engineering, Federal Institute of Science and Technology, Angamaly, Kerala, India*

ARTICLE INFO

Keywords:
Ground penetrating radar
Signal analysis
Stone masonry
Anomaly identification
Dam deterioration

ABSTRACT

The mega stone masonry (SM) structure of dams saves water for human needs but requires rehabilitation due to age, hydrological, and natural deterioration. However, there are no scientifically proven methods for identifying air cavities resulting from mortar loss in the SM. This study aims to predict and assess hidden air cavities in the Dam using a Ground Penetrating Radar (GPR) survey and an advanced data-processing technique incorporating the Continuous Wavelet Transform (CWT) with Time-Energy Density Analysis (TEDA). The proposed technique overcomes the interpretative shortcomings of traditional B-scan radargrams by efficiently localising non-stationary GPR signals in the time-frequency domain and extracting valuable energy-decay characteristics. TEDA quantitatively distinguishes air cavities from dense inclusions, such as stone boulders, by analysing regions where the signal energy shows localised enhancement. Air-filled voids show negative decay coefficients because transient interference and localised energy reinforcement occur within the low-loss air space. In contrast, solid inclusions exhibit positive decay coefficients due to progressive energy loss in high-dielectric, lossy materials. This distinction allows TEDA to separate features that would otherwise produce overlapping or indistinguishable hyperbolic signatures in conventional GPR data. Field surveys were conducted on a masonry-gravity dam in Karnataka, India, along sections of its spillway and crest. A stone masonry model with a predefined cavity was also studied for evaluating the efficacy of our detection methods and processing tools under controlled conditions. Small-scale air cavities, together with regions of mortar deterioration at shallow depths, were identified in GPR surveys by creating 2D scatter plots of energy peaks that highlighted clusters of negative decay coefficients. The results were verified through Multichannel Analysis of Surface Waves and by borehole coring, further confirming the validity and accuracy of the TEDA-CWT technique. Besides detection, the proposed method can spatially quantify subsurface air cavities, providing actionable insights for engineers to plan targeted remedial treatments such as grouting.

1. Introduction

The integrity and safety of dams are critical to water resource management, as many of these structures have been in operation for several decades and require continuous maintenance. Most stone masonry (SM) dams are susceptible to gradual deterioration due to ageing, hydraulic loading, material degradation, and environmental exposure. This degradation affects all major structural components of the dam, including the spillway, crest, slopes, and foundation, primarily through the progressive breakdown of joints and the resulting instability in SM structures. The spillway, often subjected to continuous water discharge and overtopping, experiences repeated hydraulic loading, cavitation, and erosion, which increase mechanical stress and degrade the surrounding mortar in SM or concrete structures [1]. Cavitation, where high-velocity water and surface imperfections create vapour cavities that collapse under pressure, produces intense shock waves that damage material surfaces, especially when collapse occurs near structural boundaries [2]. As a result of ageing, seismic events, or foundation settlement, the crest can develop longitudinal cracks and joint separation, which serve as avenues for water entry, accelerating internal deterioration. Masonry dam slopes, especially the upstream face, are continuously subjected to hydrodynamic and hydrostatic wave pressures. Continuous wave impact on the surface of SM and slopes can induce strain and create voids, which, in turn, form seepage paths,

---

* Corresponding author.
E-mail addresses: panjamik@iisc.ac.in (K. Panjami), anbazhagan@iisc.ac.in (P. Anbazhagan).

https://doi.org/10.1016/j.conbuildmat.2026.145910
Received 24 June 2025; Received in revised form 12 February 2026; Accepted 8 March 2026

Table 1
Case studies of applying geophysical methods in dam safety assessment.

Area	Name of the Dam	Aim of Investigation	Applied Geophysical Method	Reference
Europe	Bielsko-Biala Water Dam	Fault detection and water flow paths	ERT, Capacitively coupled resistivity, GPR	Golechowski et al. [10]
USA	Hydroelectric Dam, Alabama	Structural integrity and hydroelectric efficiency	GPR Survey	Bigman and Day [11]
China	Concrete-face rockfill Dam, Yunnan Province	Leakage detection	GPR Survey	Li et al. [12]
Greece	Marathon Dam	Quality assessment post-earthquake	Seismic, electrical tomography, GPR	Karastathis and Karmis [6]

reducing the inter block bond and promoting the development of air cavities or seepage channels below the surface. Downstream weak surface leading to a warm climate and environmental exposure leads to surface erosion and block displacement in SM structures lacking sufficient protective cladding or drainage layers [3].

Dam service life can be significantly prolonged through proper repairs and scientific retrofitting. The first requirement of an efficient retrofitting is the investigation and quantification of weak zones. Proper detection, classification, and tracking of these surface and subsurface anomalies are thus critically required to determine the overall structural soundness of the dam and to formulate preventive maintenance and rehabilitation measures. Geophysical methods offer the advantage of providing continuous spatial coverage and non-invasive evaluation, capabilities that are often lacking in traditional core sampling and visual inspection approaches. Non-destructive geophysical techniques, such as Ground-Penetrating Radar (GPR), Electrical Resistivity Tomography (ERT), and Acoustic Travel-Time Tomography (ATTT), are increasingly used to detect concealed defects without interfering with dam operations [4,5]. These methods provide extensive information on material discontinuities and moisture status without the need for extensive physical excavation or drilling, allowing engineers to identify areas of highest priority for repair, evaluate long-term performance, and reduce risks of disastrous failure [6–9]. Various case studies of applying geophysical methods to the dam safety assessment of masonry dams are summarised in Table 1.

Compared to other geophysical methods, GPR is the simplest and most effective for covering a wider area across different dam sections, as it can identify surface-level air cavities, fractures, and concealed conduits in the dam body and foundation. Karastathis and Karmis [6] utilised GPR to evaluate the condition of the Marathon Dam, inspect external marble paving, and detect subsurface flaws. The radar effectively mapped areas of dielectric discontinuities, which subsequently aligned with potential seepage routes and buried features such as old conduits. Masonry structures usually exhibit low electrical conductivity and moderate dielectric permittivity, allowing radar signals to penetrate several meters, depending on moisture content and composition. As a radar pulse hits an anomalous cavity filled with air, water, a stone boulder, or corroded steel, it alters the dielectric properties, leading to a returned signal. These can then be analysed to identify and define anomalies. Through successive survey lines in orthogonal directions and three-dimensional (3D) reconstruction, engineers can visualise subsurface anomalies with high precision in terms of shape and orientation; however, this process can sometimes lead to confusion between air cavities and stone boulder sections, as both exhibit similar hyperbolic features.

Glover's [13] study demonstrated that high-amplitude reverberations produced within an air cavity can be used to estimate its width. Air cavities within or behind dense masonry can act as transient electromagnetic interference zones during a GPR survey. The pronounced permittivity contrast at the masonry air interface generates strong reflections from both the upper and lower boundaries of the cavity. These multiple reflections undergo partial phase reversals and overlap in time, resulting in short-lived interference patterns that momentarily reinforce the local electromagnetic field. Although true standing waves cannot form under the pulsed, non-stationary conditions of GPR, the resulting reverberations can trap energy within the cavity for a brief duration, producing transient amplitude enhancement, phase modulation, and weak dispersive effects in the recorded signal [14–18].

However, to accurately identify reverberation zones and subtle internal features, advanced signal-processing techniques are required, which may not be achievable with conventional GPR data-processing methods. Data processing and interpretation during the characterisation of GPR anomalies generally entail examining radargrams for amplitude variations, phase shifts, and changes in arrival times. Attribute analysis, migration, and time-slicing techniques can further improve interpretability. In the work of Xu et al. [19], GPR was employed to delineate internal erosion features, such as burrows and voids, within earthen and concrete dams. The authors highlighted the use of signal processing to improve target visibility, including frequency filtering, background subtraction, and gain control, to separate anomaly signatures from the noise background. New developments have improved GPR's ability to identify air cavities behind concrete linings. Harseno et al. [20] conducted an extensive study assessing GPR signal interference caused by air cavities behind concrete linings. Their study demonstrated that cross-correlation analysis is effective for detecting air cavities and determining their sizes. They further proposed a new method for estimating the thickness of air cavities by measuring the apparent time delay of partially overlapping electromagnetic wave reflections within them. Most of the above surveys rely on B-scan radargrams, and feature extraction is performed by analysing the patterns. So, a different approach to material characterisation is required to clearly differentiate air cavities from other anomalies, and this paper aims to address this issue.

Recent advances in computational methods, data processing algorithms, and machine learning are increasingly being applied to enhance the accuracy and efficiency of geophysical survey data interpretation [21]. Present research highlights challenges in conventional GPR survey data processing for the characterisation of subsurface anomalies in SM dam structures. We propose a methodology to categorise anomalies using advanced data processing of GPR electromagnetic waves. Modern signal processing methods, including the Continuous Wavelet Transform (CWT) and Time-Energy Density Analysis (TEDA), are applied to improve the accuracy of identifying subsurface features of stone masonry. CWT offers flexible time-frequency analysis, making it particularly effective for interpreting the complex, non-stationary signals typical in GPR data. Energy peaks are extracted from the TEDA plots, and a trend is observed in the sign of decay coefficients between each peak pair for characterising subsurface features, especially to avoid the misinterpretation of the presence of stone boulders as air cavities. Plots were generated to clearly show the anomaly section using the opposite-sign concept of energy decay for boulders or dense inclusions and air cavities. A masonry model was constructed to validate the results using known SM structures, and field studies were conducted to survey various sections of a masonry-gravity dam (including the spillway and crest) in Karnataka, India. Geophysical investigations of the various dam sections revealed small air cavities and shallow-depth weaknesses that could potentially compromise the SM structure's integrity. GPR findings were further compared with subsurface profiles by conducting a MASW (Multichannel Analysis of Surface Waves) survey and in-situ drilling and coring. This study underscores the crucial role of geophysical methods in dam safety management, offering detailed subsurface insights vital for proactive maintenance, risk assessment, and the long-term resilience of

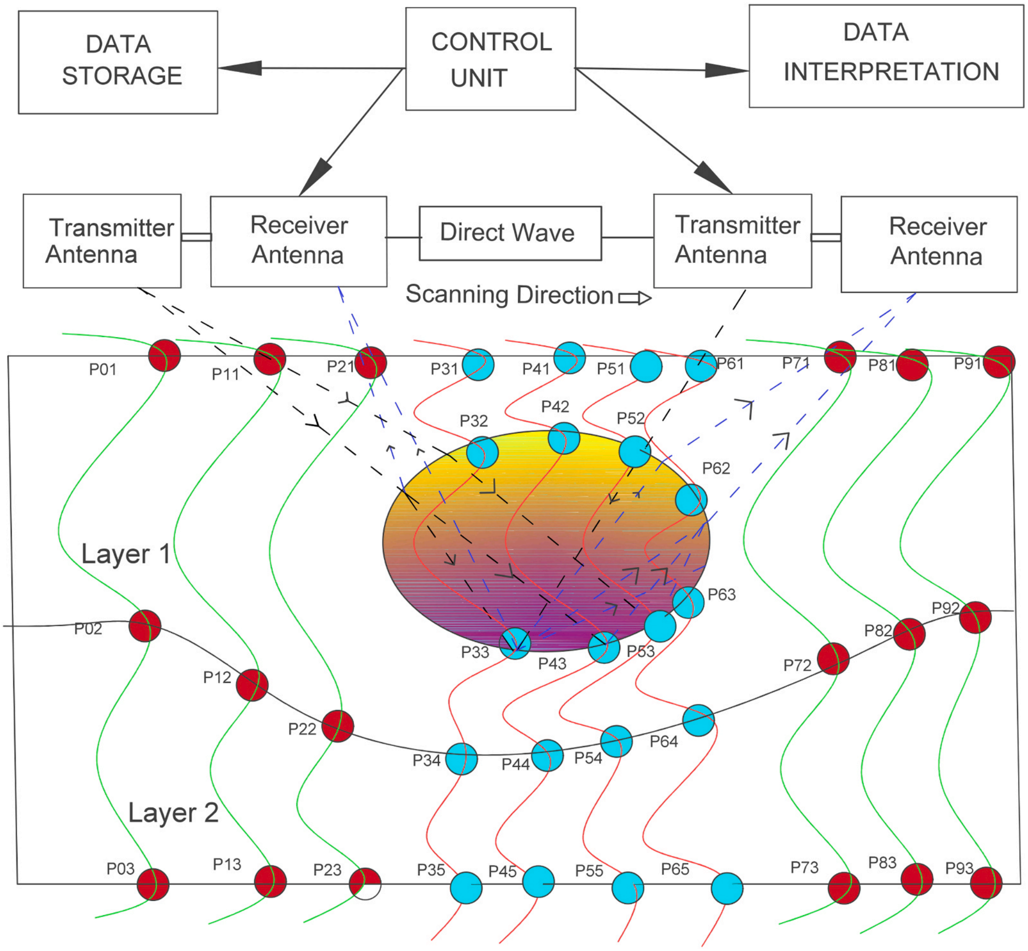

Fig. 1. Working principle of GPR in the presence of air voids with energy density peaks at layer interfaces, shown in red (no cavity) and blue (with cavity).

dam infrastructure.

2. Methodology

In GPR signal propagation, the presence of air-filled cavities in SM or concrete structures dramatically alters the energy pattern of electromagnetic (EM) waves due to strong dielectric discontinuities and multiple reflections at cavity boundaries. Air, with a much lower dielectric constant (permittivity of 1) than concrete or masonry (typically around 6), creates a substantial impedance mismatch leading to a high reflection coefficient at the air–solid interface. As a GPR pulse travels into such an air cavity, much of the wave energy is reflected toward the receiving antenna. Still, some of it might travel through the cavity and reflect at the far boundary. These repeated reflections between the upper and lower boundaries of the air cavity create an effect referred to as multi-path or reverberating reflections, in which the EM wave reflects several times inside the cavity before getting attenuated [14–17,22]. A schematic diagram of the above concept is depicted in Fig. 1. This phenomenon creates local energy build-up in the radar trace, expressed as extended or enhanced reflection patterns in the time-domain signal. In time-frequency transforms, e.g., TEDA-CWT, this energy accumulation manifests as a patch of high-energy coefficients centred on specific time scales, often serving as a unique signature that distinguishes air cavities from other features, such as stone or dense inclusions. The cyclical behaviour of the reflections can also create phase shifts and frequency-dependent interference patterns, further accentuating the presence of the void through signal-processing methods [13,23,24]. As a result, these energy accumulation zones become particularly important for anomaly detection in masonry dam surveys. Detecting and analysing these clusters of energy not only helps identify the presence of air cavities, but can also help to infer their size and even how much they might destabilise the dam.

Survey data were acquired using a GPR antenna recording time-series radar traces, representing variations in the dielectric properties of the materials beneath the surface. To ensure the accuracy and reliability of these signals, the raw data were preprocessed before any analytical transformation was performed. This preprocessing involves three key stages: static correction, background removal, and gain compensation. Static correction adjusts for discrepancies in trace start times caused by uneven antenna positioning or surface undulations, aligning the signals to a uniform temporal baseline. Background removal then eliminates consistent, non-informative reflections, such as antenna ringing or SM surface responses, which would otherwise obscure reflections from deeper cavities or inclusions. Gain compensation follows, applying a time-varying amplification factor to counteract the natural attenuation of the electromagnetic signal as it propagates through the SM structure, thereby improving the visibility of coherent cavity-related responses while preserving relative amplitude trends.

After pre-processing, a single-channel signal is extracted from the dataset for detailed analysis. This selection allows for focused investigation of the signal characteristics associated with a specific scan line or region of interest. The refined signal was then analysed using Wavelet Analysis, which is particularly useful for non-stationary signals such as GPR traces [25]. For this, CWT is applied to decompose the signal into multiple scales, capturing both high and low-frequency components. Unlike traditional Fourier analysis, the CWT provides time–frequency localisation, making it particularly effective for identifying transient features such as cavity boundaries [18]. The signal is decomposed into

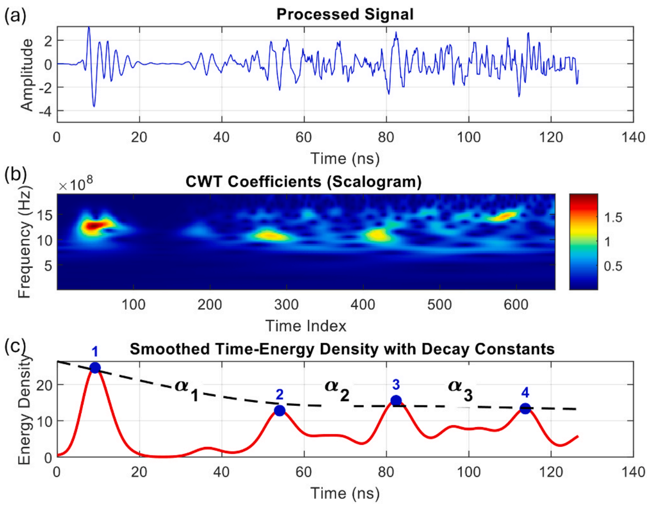

Fig. 2. (a) Single trace of a processed signal, (b) Continuous Wavelet Transform (CWT) coefficients (scalogram), and (c) smoothed time-energy density with decay constants α₁, α₂, and α₃ annotated near the fitted curve.

several sub-signals, including approximation coefficients (CA) that represent low-frequency trends, and detail coefficients (CD) that capture rapid fluctuations associated with anomalies or material interfaces. These decomposed components are then reconstructed to highlight frequency bands most sensitive to cavity detection, effectively isolating the reflections caused by discontinuities in the SM structure.

The reconstructed signal thus provides a cleaner, more interpretable profile for subsequent quantitative analysis. Following this, in the CWT–TEDA stage, we converted the decomposed signal into an energy distribution in the time–frequency domain. This energy mapping enables the detection of sharp peaks corresponding to abrupt dielectric contrasts, typically indicating air cavities or stone inclusions. By quantifying temporal variations in local energy, the TEDA framework provides a robust foundation for subsequent identification and classification of subsurface anomalies. In Fig. 1, a two-layer subsurface is shown with an air cavity inside. Red dots (e.g., P01, P02, P03) indicate the energy density peaks identified at layer interfaces where no cavities are present beneath. Similarly, in the presence of cavity sections, the peaks are marked in blue (for example, P31, P32, P33, P34, P35).

CWT was computed for each processed signal trace $x(t)$, utilising an appropriate wavelet function $\psi(t)$, such as the analytic Morlet wavelet ("amor"), which was selected for its favourable balance between time and frequency localisation when analysing oscillatory signals. The CWT is defined as:

$$W(a,b) = \frac{1}{\sqrt{|a|}}\int_{-\infty}^{\infty} x(t)\psi^*\left(\frac{t-b}{a}\right)dt \tag{1}$$

where $W(a,b)$ denotes the wavelet coefficients, a and b represent the scale and translation parameters, respectively, and ψ^* is the complex conjugate of the mother wavelet. These coefficients provide a comprehensive description of the signal's energy distribution across both the time and frequency domains [25–27]. To complement the CWT-based energy analysis, a preliminary multiresolution decomposition using the Discrete Wavelet Transform (DWT) is performed. This multi-scale framework underpins the transition to TEDA-CWT for improved time-frequency resolution. After the transformation, the time-energy distribution is derived by computing the squared magnitude of the wavelet coefficients:

$$E(a,b) = |W(a,b)|^2 \tag{2}$$

which quantifies the signal's energy at each scale a and position b. The total energy density for each trace is then obtained by summing across all scales:

$$E(t) = E_a|W(a,b)|^2 \tag{3}$$

To enhance the interpretability of the energy profile, a Gaussian smoothing filter is applied:

$$E_s(t) = G(E(t),\sigma) \tag{4}$$

where $G(E(t),\sigma)$ represents the smoothed energy density using a Gaussian kernel with standard deviation σ [28]. Processing of a single trace is depicted in Fig. 2. In this Figure, 2(a) shows the processed signal after preprocessing steps, and Fig. 2(b) represents the CWT coefficient scalogram calculated based on Eq. 2. The total energy density is calculated using Eq. 3, and Gaussian smoothing, as defined by Eq. 4, is applied to identify boundary interfaces. A smooth curve is plotted with high-energy-density points, and peaks are identified as shown in Fig. 2 (c). The decay coefficient α is derived by applying the logarithmic form of the exponential decay law. Assuming two energy peaks at the time positions t_1 and t_2, with corresponding energy densities E_{t1} and E_{t2}, the coefficient is given by:

$$\alpha = \frac{\ln(E_{t1}) - \ln(E_{t2})}{t_2 - t_1} \tag{5}$$

Following the computation of the decay coefficient α from the TEDA–CWT framework, its variation provides valuable physical insight into the electromagnetic wave character of the masonry medium. The coefficient reflects the relative rate of change in electromagnetic energy density as the GPR wave propagates through the structure. Positive values of α represent the signal attenuation arising from dielectric and conductive losses within the solid matrix [29,30]. In these regions, the electromagnetic energy density decreases monotonically with distance as the radar pulse is progressively absorbed and scattered, resulting in a consistent positive attenuation coefficient ($\alpha > 0$). This behaviour is typical for dry concrete mortar with dielectric permittivity ranging from 5 to 8 and stone blocks such as asphalt, granite or basalt inside the concrete medium with dielectric permittivity ranging from 3 to 8 [31]. The dielectric contrast is moderate in this case, with the reflection coefficient varying from a minimum of zero to a maximum of 0.24, and the energy follows an exponential decay pattern:

$$u(z) = u(0^+)e^{-2\alpha z} \tag{6}$$

Eq. 6 is governed primarily by intrinsic material losses [29,30]. Here, $u(0^+)$ denotes the energy immediately below the mortar–stone interface, representing the transmitted component of the electromagnetic wave. And, the term $e^{-2\alpha z}$ expresses the exponential attenuation of this energy with depth due to dielectric and conductive losses within the medium.

In contrast, when the propagating GPR wave encounters an air-filled cavity with a dielectric permittivity of 1 within the concrete mortar, the large dielectric discontinuity at the mortar–air interface with a reflection coefficient varying from 0.45 to 0.50 generates a strong reflection, while the subsequent air–mortar boundary produces a secondary, non-reversed reflection. The overall electromagnetic field within the cavity can be described as the superposition of forward and backward travelling waves [32] as expressed in Eq. 7.

$$E_{\text{total}}(z,t) = E_0\left(e^{-j\beta z} + \Gamma e^{j\beta z}\right)e^{j\omega t} \tag{7}$$

Where e^{jwt} denotes the time-harmonic factor describing oscillation at the angular frequency.

$$|E_{\text{total}}(z,t)|^2 = E_0^2\left[1 + |\Gamma|^2 + 2|\Gamma|\cos(2\beta z + \phi)\right] \tag{8}$$

Eq. 8 represents the instantaneous energy density where ϕ is the phase shift between reflections from the upper and lower interfaces and Γ is the reflection coefficient. When $\phi \approx 0$, these reflected components interfere constructively, producing transient reinforcement of the electromagnetic field near the lower interface. Because air is nearly lossless,

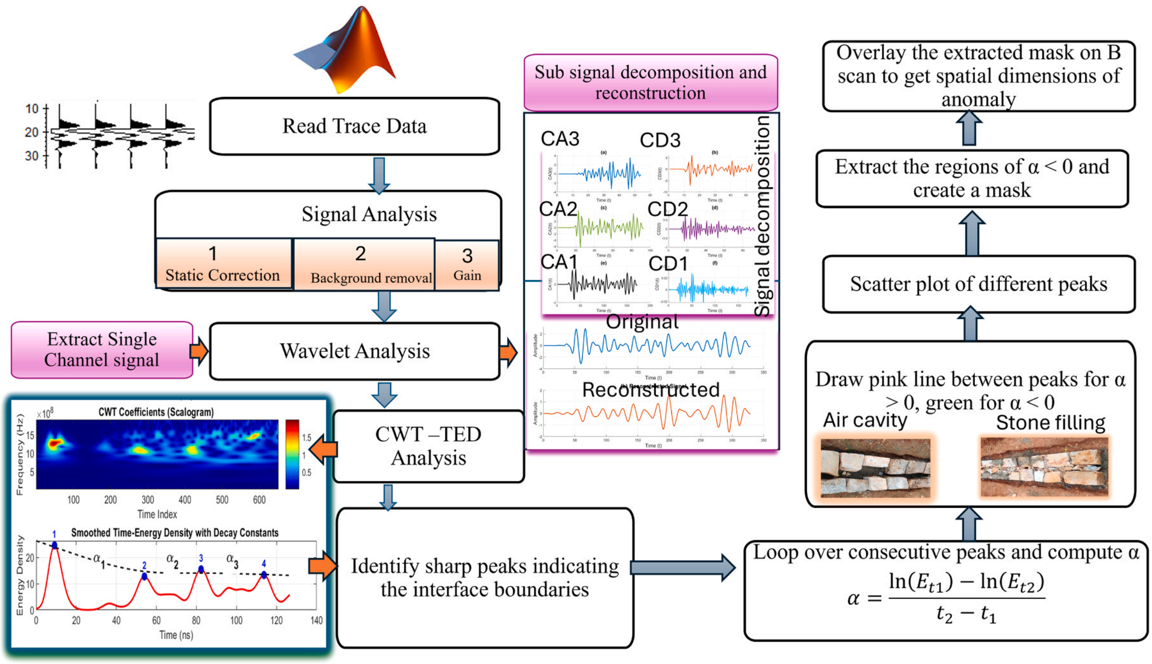

Fig. 3. Flowchart of the algorithm used in the study.

this interference can result in localised energy accumulation or oscillatory variations in the field strength within the void. While the true standing waves cannot form under the pulsed, non-stationary conditions of GPR operation, these short-lived interference effects can momentarily amplify the recorded energy amplitude at specific depths. When gain is applied, this amplitude enhancement becomes more pronounced, improving the visibility of deeper reflections but also magnifying such transient interference effects. Consequently, the instantaneous energy density $u(z)$ may increase locally before decaying again, yielding apparent negative slopes in the time-energy decay curve. After analysing the individual traces for energy density curves, 2D scatter plots are generated, and lines are plotted between different peaks using the condition of a pink colour for alpha greater than zero and a green colour for alpha less than zero, as shown in the algorithm flow chart in Fig. 3. The green colour cluster regions are extracted as an anomaly mask. While the decay coefficient mask is computed in the time domain (with time as the vertical axis), the B-scan images are displayed in the depth domain. To ensure accurate overlay and interpretation, a time-to-depth transformation was applied using the relation depth = (v × t) / 2, where t is the two-way travel time and v is the radar wave velocity in the medium.

Subsequently, the area calculation procedure was implemented to quantify the extent of the detected anomalies. The negative decay regions obtained from the TEDA–CWT analysis were thresholded to generate binary masks representing anomaly zones in the time–distance (B-scan) domain. The time axis was then converted to depth using the

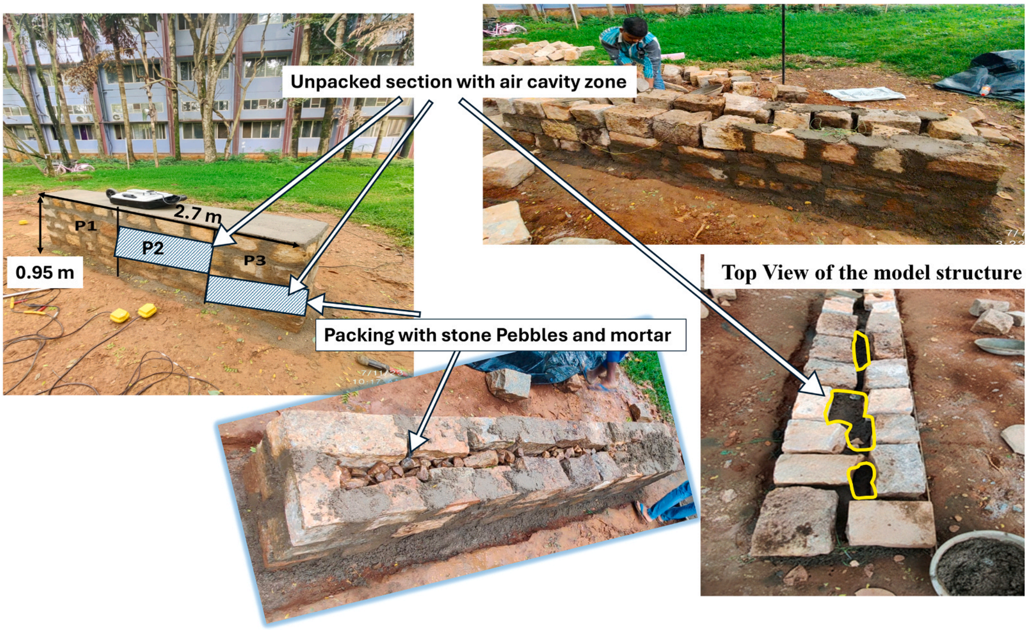

Fig. 4. Model masonry structure constructed in the IISc campus with cross-section details showing sections of packed and unpacked regions.

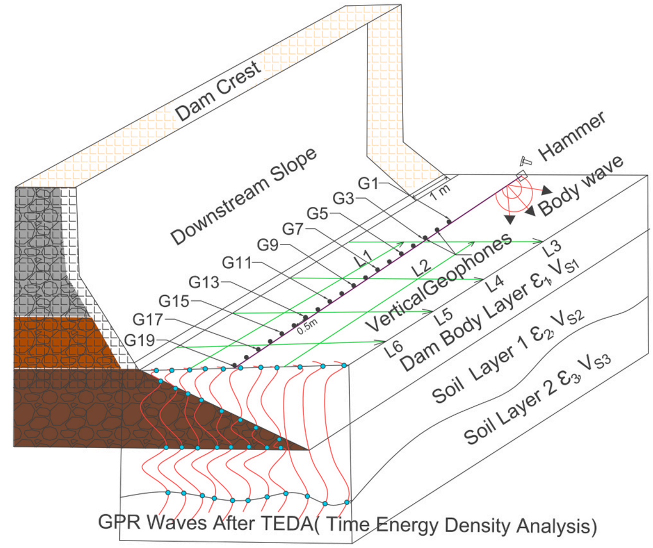

Fig. 5. Schematic diagram of dam sections showing typical alignment of GPR and MASW surveys for the spillway region.

previously defined velocity model. Each pixel within the binary mask was assigned its corresponding real-world spatial dimensions, with the horizontal scale determined by the GPR trace interval and the vertical scale derived from the time-to-depth conversion. Finally, the total area of each anomaly was computed as the sum of all pixels within the masked region multiplied by their corresponding areas, providing a quantitative measure of the subsurface anomaly size. The entire data processing was done using MATLAB code, and the algorithm's flowchart is shown in Fig. 3.

3. Experimental investigation

3.1. Data acquisition

The GPR device used in this study was the MALÅ GX system from MALÅ Geoscience, intended for high-resolution subsurface imaging. The system was equipped with bi-static, shielded, ground-coupled antennas, which are particularly effective at reducing external noise and enhancing the quality of subsurface reflections. Three antennas with central operating frequencies of 160 MHz, 450 MHz, and 750 MHz were utilised in this study, in various cases, to balance depth of penetration and resolution. The 160 MHz lower-frequency antenna offered greater penetration, enabling the observation of larger features at greater depths, often reaching approximately 8–12 m in favourable conditions. However, in real field settings with moisture or clay-rich soils, the effective depth is usually less. The higher frequencies (450 MHz and 750 MHz) offered higher resolution for shallow targets; the 450 MHz antenna typically achieves depths of about 3–5 m, and the 750 MHz antenna works for depths of around 1–3 m. These antennas were wired to the MALÅ GX controller unit and powered by an odometer wheel, which provides precise distance data during data acquisition. The bi-static setup, in which the transmitter and receiver are placed in separate compartments, helped minimise antenna ringing and improve the signal-to-noise ratio. The shielded nature of the antennas prevented electromagnetic energy from radiating downward into the ground, reducing interference from nearby sources, a significant benefit in circumstances involving surface clutter or reinforced concrete. The system's high dynamic range (HDR) capability and high data-acquisition rate also enhanced data quality, rendering it exceptionally adept at void detection under concrete structures, such as stone masonry dams.

3.2. Masonry model structure

A model masonry structure (Fig. 4) was built inside the IISc campus to clearly understand the trend in decay coefficients and to validate the sign convention of decay coefficients in the presence of air cavities. The structure had a length of 2.7 m, divided into three sections, and a width of 0.9 m and a depth of 0.95 m. Boulder stones and air cavity sections, in the form of packed and unpacked regions, were inscribed in the model, and GPR surveys were conducted using a 750 MHz antenna in time-domain acquisition mode to understand the trend in decay patterns across the sections. The reason for using 750 MHz is the masonry model's shallow depth and the need to increase resolution to identify anomalies in the masonry.

3.3. Field investigation in dam sections

A typical dam cross-section is depicted in Fig. 5, with the GPR survey gridlines marked in green and the MASW field survey setup. MASW surveys and boreholes were conducted at selected sections for validation of GPR results. The acquired GPR traces were subsequently converted into energy-density plots. For the spillway sections, Time-Energy Density Analysis (TEDA) waveforms are illustrated as red traces in Fig. 5, representing typical (intact) conditions. In regions containing air cavities, corresponding variations are expected to appear in the energy density plots.

The spillway section selected for the study was a masonry dam in Karnataka state, India. It was a gravity dam built using random rubble stone and surki mortar. The immense force of water gushing through the dam’s spillway exerts continuous pressure on the masonry structure. Over time, this relentless flow erodes the surki mortar that binds the masonry stones, gradually weakening the spillway section. The survey employed ground-coupled GPR antennas with central frequencies of 450 MHz, 750 MHz, and 160 MHz, along with a GPR acquisition unit, interconnecting cables, and an odometer. The measurements were carried out in single-channel, continuous-wheel acquisition mode. The damaged section of the dam spillway was at the downstream toe, and surveys were conducted in a grid pattern. Survey gridlines for the spillway section are marked as shown in Fig. 5. The acquisition parameters while doing a GPR survey in the dam spillway were set to a 46.875 ns time window and 240 samples per trace, ensuring optimal resolution for the survey. With a sampling frequency of 5120 MHz, the resulting Nyquist frequency was 2.56 GHz, making it well-suited for this investigation. The antenna separation was 0.18 m, and the measurement was carried out with a fixed increment of 0.3 m, facilitating consistent data collection across the surveyed section. To preserve the integrity of the recorded signals, no additional preprocessing was applied during data acquisition, ensuring that the raw signal remained unaltered for subsequent analysis. The survey utilised a distance interval of 0.008573 m, allowing precise spatial calibration. Additionally, a 0.5-meter marker was used to correct positions, ensuring that the recorded data were accurately rescaled from a time-based format to an evenly spaced dataset.

A survey was also conducted along the crest of a gravity dam consisting mainly of random rubble masonry bonded by lime-based surki mortar, a classic composite of lime, brick dust, and sand characterised by its strength and resistance to water. The site is primarily composed of a mixture of sedimentary deposits, including clay, silt, and sand layers, interspersed with gravel and occasional boulder formations. These sediment layers display varying degrees of compaction and cementation, contributing to the heterogeneous nature of the subsurface. Additionally, the site features bedrock formations of metamorphic origin, such as schist and gneiss, which provide a stable foundation in some areas but also introduce zones of weakness from fractures or weathering. The cross-sectional profile of the dam was trapezoidal to withstand hydrostatic pressure through its own weight. The upstream face was inclined slightly to minimise uplift pressure, and the downstream face was

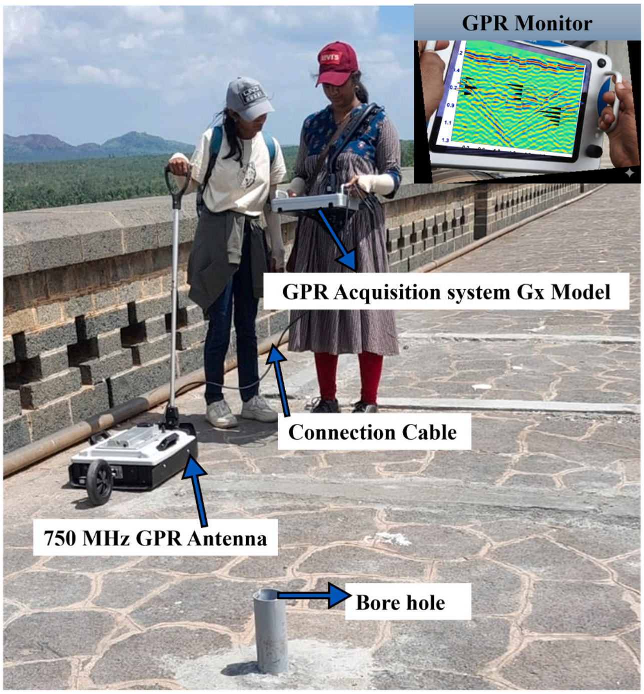

Fig. 6. GPR field survey image in the dam crest section.

stepped to dissipate overflow energy. The dam was constructed in successive horizontal layers, with each course meticulously keyed into the one below to improve monolithic behaviour. A GPR survey was carried out across the entire crest region to identify weak zones. A typical field photo of a GPR survey in the crest dam section is shown in Fig. 6.

A MASW survey was conducted alongside core drilling to confirm the GPR results. A typical field photo of a MASW survey is shown in Fig. 7.

MASW is a seismic survey method commonly used to monitor dam safety, helping assess the subsurface and pinpoint potential weak spots. It involves creating surface waves using a seismic source, such as a sledgehammer hitting a metal plate or a rubber pad. A series of geophones, set up in a row, captures the surface waves as they move along the ground. The collected wave data is processed to measure phase velocities at different frequencies, forming a dispersion curve that shows the relationship between frequency and phase velocity. By inverting this curve, one can produce a 1D or 2D shear-wave velocity profile that reveals the subsurface's stiffness and highlights problematic areas, such as unstable layers or weak zones. MASW offers efficient and detailed profiling, enabling proactive maintenance [33,34]. The MASW survey helps investigate paleochannels suspected to provide a passage for leakage from a dam, identifying low S-wave velocity anomalies as drainage [34]. The present survey employed a 12-channel seismograph

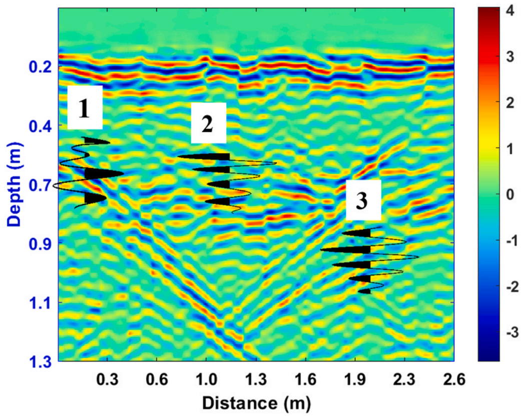

Fig. 8. B-Scan radargram of model structure with waveforms depicted for specific regions showing positive(section1) and negative (Section 2 & 3) polarity.

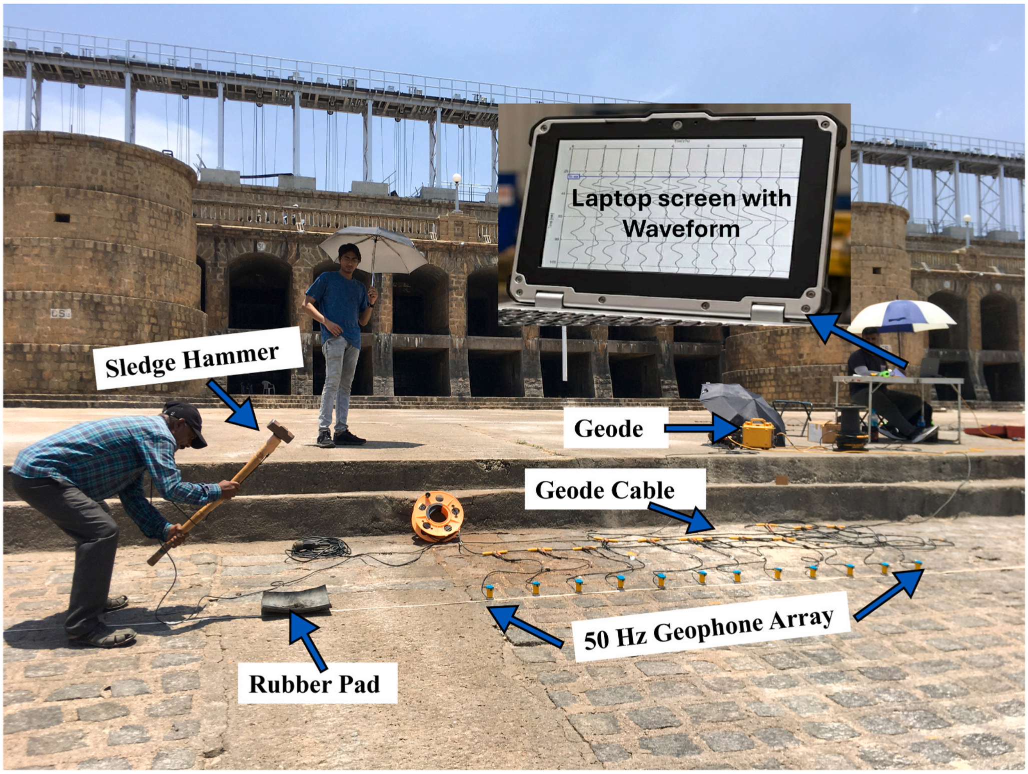

Fig. 7. Field MASW survey image at the dam spillway section.

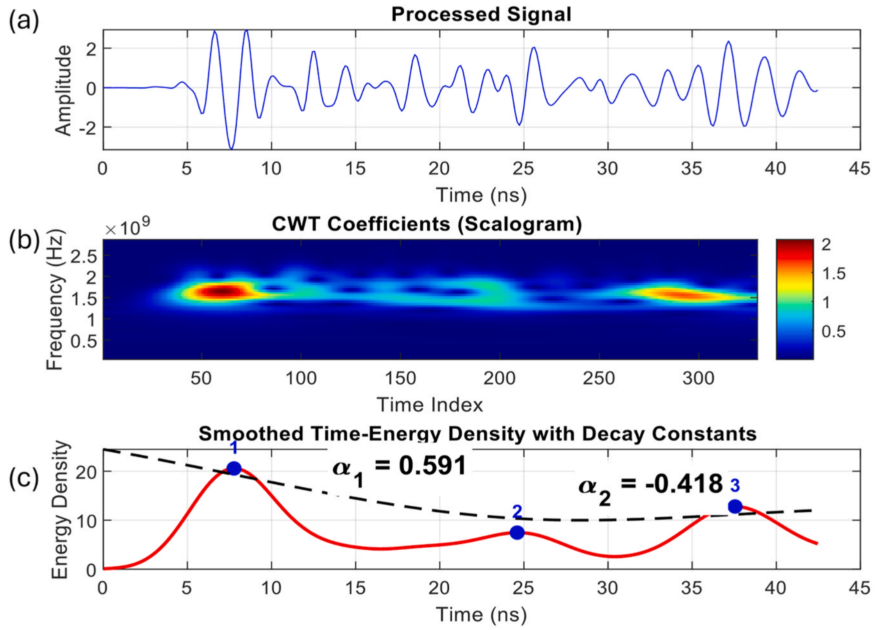

Fig. 9. (a) Processed GPR trace 236 of model structure, (b) Continuous Wavelet Transform (CWT) coefficients (scalogram), and (c) smoothed time-energy density with decay constants annotated near the fitted curve.

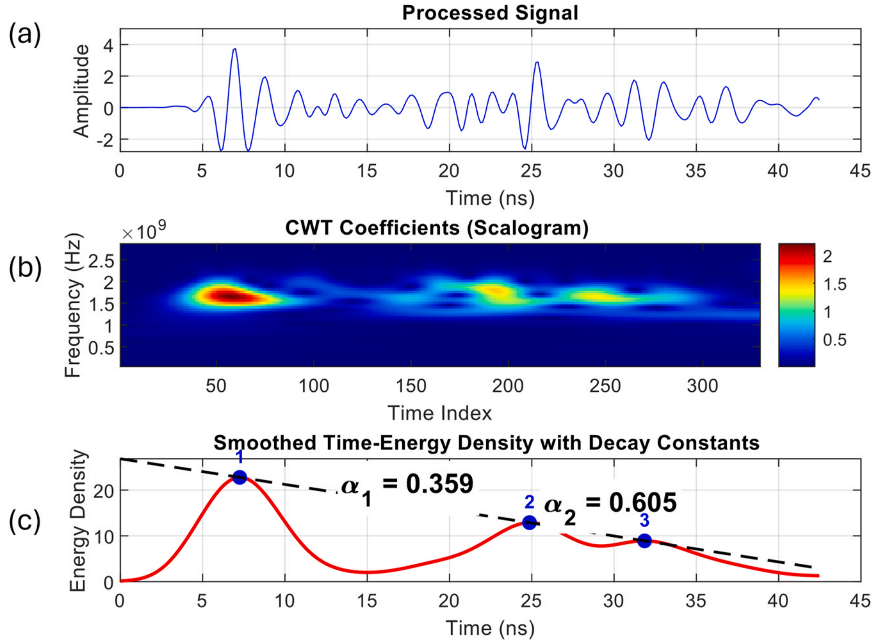

Fig. 10. (a)Processed GPR trace 320 of model structure, (b) Continuous Wavelet Transform (CWT) coefficients (scalogram), and (c) smoothed time-energy density with decay constants annotated near the fitted curve.

with geophones operating at 50 Hz.

4. Results and discussion

4.1. Anomaly detection in masonry model structure

The B-Scan radargram obtained from the GPR survey after DC removal, background filter and automatic gain control is shown in Fig. 8, with waveforms from specific regions highlighted, showing both positive and negative reflections based on phase reversal of the signal. Waveform marked as 1 in Fig. 8 indicates the positive wave reflection, and 2 and 3 represent the negative reflections. Analysing individual wave reflections is complex, and a new methodology has been developed to reduce the complexity.

Performing TEDA with CWT on individual GPR A scans in a total of 605 traces in the source file, typical results of traces 236 and 320, respectively, are shown in Figs. 9 and 10, which reveal that the traces exhibit negative decay coefficients. Selected traces are plotted in Fig. 11 (a). The blue dots with numbers indicate the boundaries between the different interfaces underneath. Decay constants were evaluated from logarithmic attenuation between peaks using Eq. 5, as described in the methodology section. In Fig. 11(a), we can see different traces with positive and negative decay coefficients. It was found that the presence of air-filled cavities results in strong negative reflectivity, causing

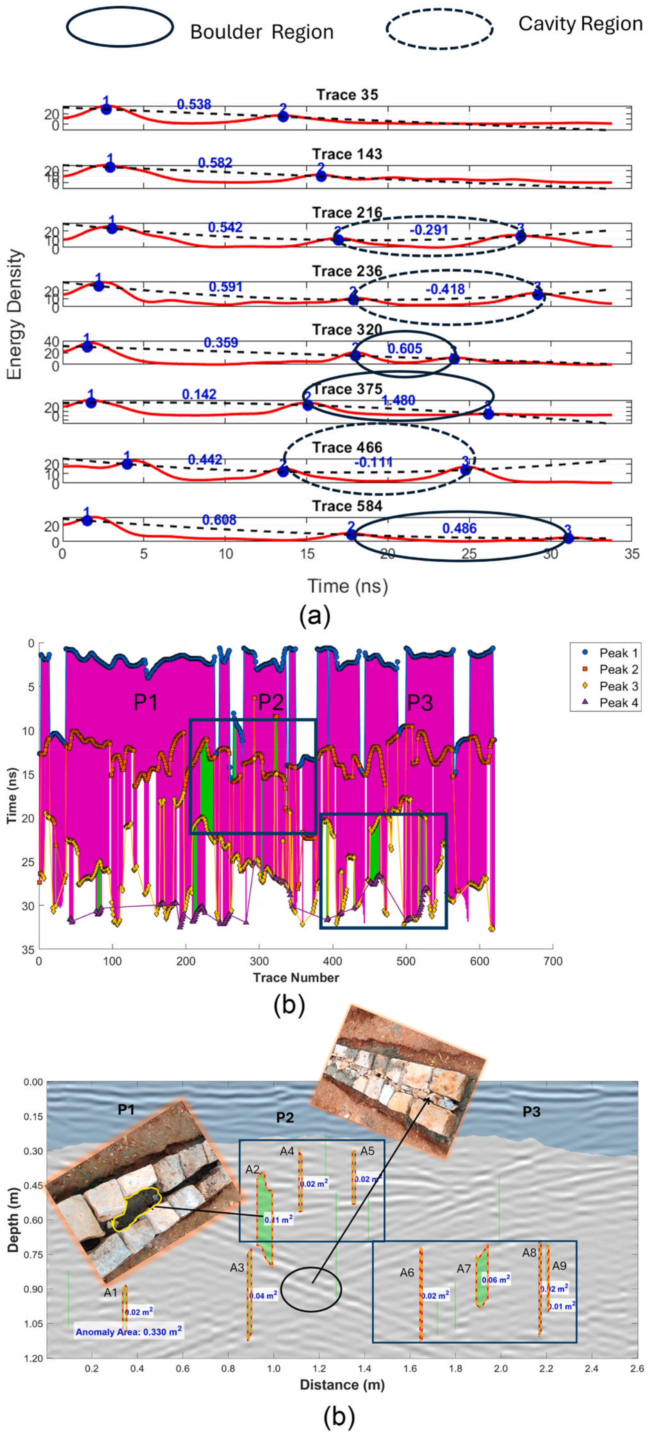

Fig. 11. (a) Time energy density plot of selected few traces of masonry model structure, (b) 2D Scatter plots of peaks with anomalous regions highlighted, (c) Anomalous sections overlaid on B scan Image in model structure using CWT-TEDA method.

transient interference with a negative decay coefficient due to the high dielectric contrast between air and the surrounding construction material, as well as multiple reflections.

In contrast, positive reflectivity with a positive decay coefficient, as shown in Fig. 11(a), suggests an interface where the dielectric permittivity of the second material is higher than the first (e.g., mortar-boulder) along with the attenuating nature of the second medium. Next, the entire anomalous sections were checked for their decay coefficients, connecting the interface peaks and the cavity sections highlighted in continuous lines and the boulder-in-mortar sections highlighted in dotted lines, as marked in Fig. 11(a). Energy peaks are extracted from the TEDA plots of all traces, and a trend is observed in the sign of decay coefficients between each peak pair for characterising subsurface features, especially to avoid the misinterpretation of the presence of boulders as air cavities. All traces are combined to create 2D scatter plots that identify clusters of negative-decay regions, as shown in Fig. 11(b). The negative regions, highlighted in green in the image, are extracted separately as an anomaly mask, and the anomaly area is calculated. Later, this anomaly mask is overlaid on the GPR B-scan image, with distance on the X axis and depth on the Y axis, to estimate the anomaly's spatial dimensions, along with the anomalous area annotated. The model constructed here was a small masonry structure with unpacked air cavities at different sections. The anomalous regions observed matched the unpacked cavity sections of the model structure for P2 and P3. These sections are extracted as an anomaly mask and overlaid on the B-scan image, as shown in Fig. 11(c), with the approximate area calculated and annotated. It can be used in the future to estimate the volume of grouting material required to fill voids in real masonry structures.

Table 2 provides a comprehensive summary of the detected air cavities and their validation against ground truth observations, which closely match the observations in Fig. 11(c) and illustrate the spatial distribution of anomalies within the investigated section. The anomalies identified range from small to large air cavities, with detected areas ranging from 0.01 m^2 to 0.11 m^2, indicating heterogeneity in subsurface conditions. Anomaly A2, with a detected area of 0.11 m^2, represents the most significant void confirmed through ground validation, highlighting the detection algorithm's effectiveness in identifying major structural defects. In contrast, anomalies such as A6 and A8, with areas of 0.02 m^2, may represent false detections due to multiple reflections from closer air cavities. The percentage error values, ranging from 4.5% to 15%, remain within acceptable bounds, highlighting the model's robustness.

Fig. 11(c) visually corroborates these findings by highlighting two prominent clusters of anomalies in sections P2 and P3, indicating potential structural vulnerability. The overall detected anomaly area was 0.333 m^2, compared to an actual area of 0.26 m^2, with an average percentage error of 8.59%, indicating a high level of agreement between model predictions and ground truth observations. Analysis of the detection performance across different depth intervals (Table 2) reveals a clear depth-dependent trend in identification accuracy. The results show that air cavities located within the intermediate depth range of approximately 0.3–0.8 m with cavity thickness of 0.1–0.3 m exhibit the lowest percentage errors, typically between 4.5% and 6.4%, as observed for anomalies A2, A4, and A5. At greater depths, such as 0.75–1.10 m, the error increases to about 13.5%, likely due to attenuation and signal dispersion that reduce sensitivity in deeper layers. Conversely, cavities located in deeper zones (0.95–1.05 m), such as A1, tend to exhibit higher errors, around 15%, possibly influenced by near-surface scattering or irregular cavity geometries that affect signal consistency. Additionally, a GPR antenna with a centre frequency of 750 MHz in a medium with a dielectric permittivity of 6, the minimum thickness of an air cavity that can be detected is 0.16 m. Here, the cavity A1 has a thickness of 0.15 m and is still being detected by the system. The reason is that cavity A1 is in soil below the masonry part, with a dielectric permittivity of 13, and it has a detection resolution of 0.11 m for the air cavity thickness. Additionally, instances of non-detection (A6 and A8) as mentioned in Table 2 occur mainly within the 0.75–1.10 m range, suggesting occasional false negatives where cavity dimensions fall below the effective detection threshold of the antenna frequency. This highlights the need to incorporate depth-dependent calibration or adaptive sensitivity adjustments to enhance further the consistency of subsurface anomaly detection across varying depths.

The detection accuracy above 90% (1 − mean error/100) suggests that the proposed method has high confidence in identifying and quantifying air cavities for the considered model structure. The

Table 2
Summary of detected air cavities and validation results for the model structure.

Anomaly ID	Section	Depth Range (m)	Detected area (m^2)	Ground Truth Feature	True Area (m^2)	Percentage Error (%)
A1	P1	0.95–1.10	0.02	Loose air cavity between the model and the soil	0.0174	15.0
A2	P2	0.4–0.8	0.11	Air cavity	0.1034	6.4
A3	P2	0.75–1.10	0.04	Loose air cavity between stones	0.0352	13.5
A4	P2	0.3–0.7	0.02	Loose air cavity	0.0191	4.5
A5	P2	0.3–0.6	0.02	Loose air cavity	0.0191	4.5
A6	P3	0.75–1.10	0.02	None detected	—	—
A7	P3	0.75–1.05	0.06	Air cavity	0.0471	6.2
A8	P3	0.75–1.10	0.02	None detected	—	—
A9	P3	0.75–1.10	0.01	Loose air cavity between stones	0.0091	10.0
A10	P3	0.75–0.85	—	Loose air cavity between stones	0.005	—
Total	—	—	0.32	—	0.2574	8.59

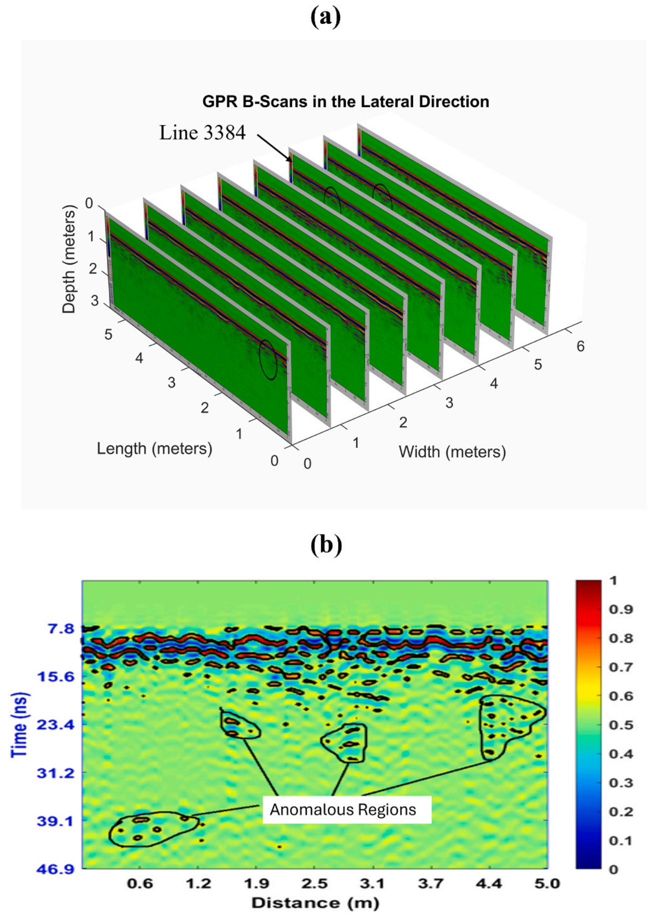

Fig. 12. (a) GPR radargrams of spillway arranged in lateral directions, (b) High threshold regions extracted from the GPR B-Scan for anomaly identification.

relatively small deviation between detected and true cavity areas indicates that the process is both sensitive and precise, particularly for cavities larger than 0.02 m^2 with a 750 MHz antenna. However, for very small anomalies, slight overestimations may occur, warranting cautious interpretation in those localised zones.

4.2. Anomaly detection in dam spillway

B-Scan images obtained with a 450 MHz GPR antenna were found to be most effective for air-cavity detection in this case, when compared to 750 MHz and 160 MHz data. GPR lines of both longitudinal and lateral directions of the spillway section with a 450 MHz antenna are processed and arranged as stacks, and suspected locations of anomalies are marked as circles in the radargrams, as shown in Fig. 12(a). Initially, both parallel X-scans and Y-scans were used to build the dataset, ensuring comprehensive coverage of the survey area. The data were processed with specific attention to the scan increment and trace differences, and interpolation was used where necessary. Processing steps included applying a DC shift subtraction to remove baseline drift and a static correction to account for time delays in the signal. A background-removal step was also implemented to reduce noise and enhance the clarity of subsurface features. The bandpass Butterworth filter frequency range was set to 100–600 MHz, which is appropriate for the expected depth and resolution of the targets.

Further refinement involved using a bandpass Butterworth filter to isolate the frequencies of interest, and a trace-averaging technique to smooth the data and reduce noise. The Kirchhoff migration was applied to correct for the diffraction hyperbola, thereby improving the spatial resolution and the accuracy of the subsurface image. The gain function settings were adjusted to enhance signal amplitude, with linear gain and exponential damping parameters set to balance the signal-to-noise ratio.

The main issue identified was the presence of subsurface boulders at certain locations. In the generated 3D GPR scans, both boulders and air cavities appeared as anomalies exhibiting hyperbolic reflections in the B-scan profiles. Therefore, it was necessary to distinguish between boulder- and cavity-induced anomalies to identify potential grouting locations accurately. One method for differentiating the boulders from the cavity region is to examine the waveforms at doubtful locations. The anomalous regions are initially marked based on the radargram high threshold and hyperbolic features, and later checked for waveform patterns at doubtful locations. Manual identification of high-threshold and hyperbolic features in radargrams can lead to human error, so automatic detection methods are used to generate echo diagrams. One such anomalous line identified from the gridline survey (Line 3384 as marked in Fig. 12a) is illustrated in Fig. 12(b), with the anomalous regions automatically delineated based on the reflection amplitude; these are known as echo diagrams. The advantage of generating the echo diagram for anomaly identification is that the high-threshold region can be highlighted based on cluster density, and later, the highlighted regions can be checked for waveforms to characterise the anomaly. From field data, it was found that there was a positive wave reflection with boulders and a negative wave reflection with cavities. However, analysing individual waveforms to differentiate between boulders and cavity regions is tedious when there are many traces.

To avoid the above complication, GPR traces were processed to create time-energy density plots using MATLAB code with the continuous wavelet transform analysis, as explained in the methodology section. It was observed that there were clusters of negative and positive decay coefficient regions in the trace data, which showed a similar kind of sharp hyperbola and high threshold regions in radargrams. The trend was confirmed using the known model structure at IISc, and the same is implemented in the field dam section. The air cavity sections identified by the GPR method with advanced CWT-TEDA analysis, as depicted in Fig. 13(a), matched the MASW results, as shown in Fig. 13(b). A total of eight sections were marked, in which Section 3 represents the identified

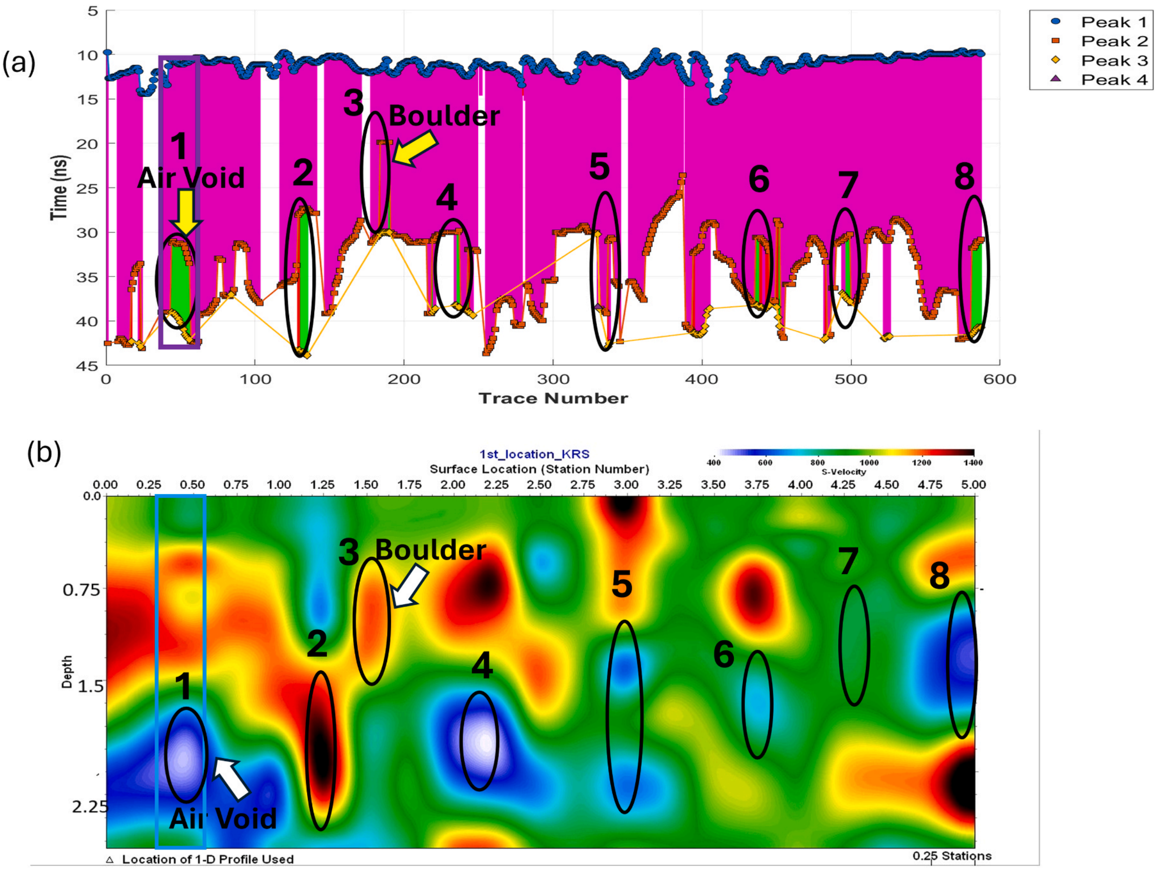

Fig. 13. Survey results of spillway section (a) 2D scatter plot of peaks highlighting anomalous region (b) 2D shear wave velocity profile of the section from MASW survey.

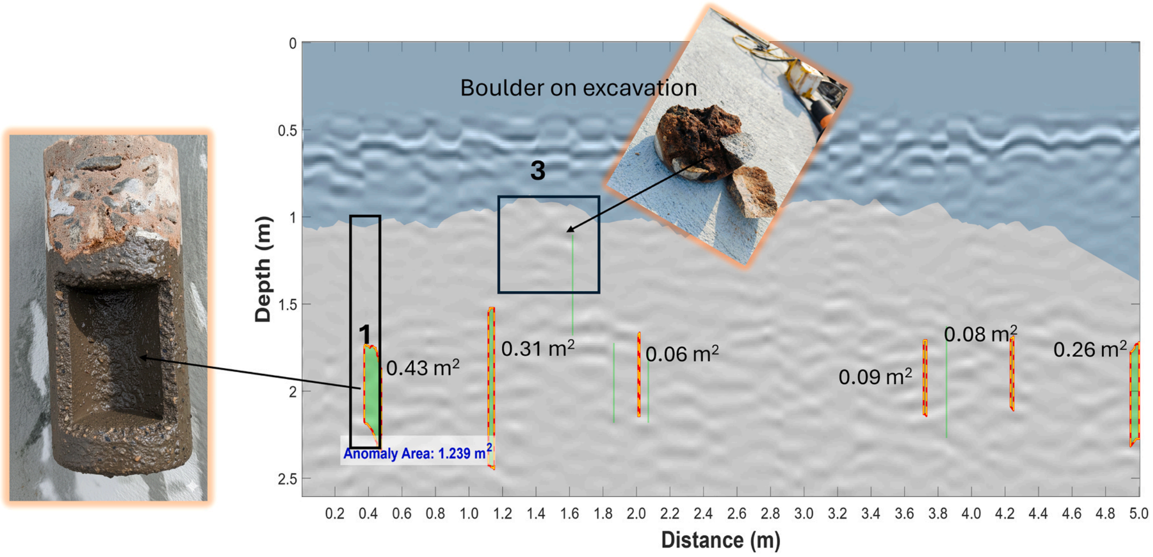

Fig. 14. B-Scan image overlaid by anomaly regions annotated with the area of anomalous sections for the dam spillway.

boulder, and all other sections indicate the air cavity. The spatial dimensions of the air cavity identified from the GPR match the shear-wave velocity profile from MASW. Coring was done in Sections 1 and 3 (marked in Fig. 13) to confirm the results, and the air cavity and boulders were identified at the corresponding locations, as marked in Fig. 14. On keen observation, it is noticed that the air cavities are formed by internal erosion due to hydraulic action. The green negative-decay-coefficient regions were extracted as an anomaly mask and overlaid on the processed B-scan image to precisely identify the spatial dimensions of the air cavity. The area of the anomalous section was calculated and annotated in Fig. 14. The layering observed in the peaks, from order, is highlighted in two shades in the B-scan image. The first dark blue colour represents the top stone masonry layer, with a thickness of around 1 m, and the second layer shows the subsurface layer with

Table 3
Spillway section core sample observations.

Depth (m)	Description	CRR (%)	Anomaly Area (m^2)
0–1.0	Stone masonry	92	–
1.0–1.7	Lime with surki mortar	93	–
1.7–2.4	Lime with surki mortar (Air cavity zone)	14	0.41
2.4–3.0	Lime with surki mortar	85	–

lime and surki mortar. The calculated anomaly area can be used to estimate the volume of grout required for the weak section.

Fig. 14 illustrates the spatial distribution of anomalies detected along the spillway section, with a cumulative anomaly area of 1.239 m^2 distributed across multiple zones at depths ranging from 1.5 m to 2.5 m. The most significant anomaly, measuring 0.43 m^2, is highlighted within the black box near the left section. Also, smaller anomalies such as 0.31 m^2, 0.06 m^2, 0.09 m^2, 0.08 m^2, and 0.26 m^2 are dispersed across the profile, indicating localised voids or weak zones within the masonry structure. A core was drilled at the location of the 0.43 m^2 anomaly to confirm the results. Table 3 reveals a substantial reduction in the core recovery ratio (CRR) to 14% between depths of 1.7–2.4 m, confirming the presence of an air cavity zone with an estimated thickness of 0.7 m and an anomaly area of 0.41 m^2, with a percentage error of 6%. In contrast, the adjacent layers (0.0–1.0 m,1.0–1.7, and 2.4–3.0 m) exhibit CRR values respectively of 92%, 93% and 85%, indicating structurally intact lime-surki mortar.

4.3. Anomaly detection in the dam crest

The processed images of the data acquired from the dam crest sections are shown in Fig. 15, revealing multiple layering patterns and anomalies between depths of 0.3 and 0.45 m. The survey findings show the heterogeneous and non-uniform nature of the surki mortar layers across the site. The anomaly highlighted in Fig. 15, measuring 0.02 m^2, occurs at a depth of 0.3–0.45 m within Layer 1. A core was drilled in the section to confirm the presence of an air cavity, and a deteriorated region was confirmed in the core measuring 0.144 m x 0.15 m, with an area of 0.0216 m^2. A percentage error of 7.5% observed between the detected area and ground truth at depths of 0.3–0.45 m (Section 2), along with its extremely low core recovery ratio (CRR) of only 10%, indicates that this zone exhibits severe deterioration. Such defects are likely caused by moisture ingress or inadequate construction practices. In contrast, adjacent layers (Sections 1, 3, 4, and 5) exhibit much higher CRR values, ranging from 88% to 95%, indicating intact, well-bonded material. This sharp variation in CRR strongly suggests localised voids and weak mortar pockets, which may affect the load-bearing capacity within this depth range.

4.4. Discussion

The proposed approach reliably identified anomalous zones within the structure in the present study, with the time-energy decay coefficient serving as a reliable indicator of potential deterioration. These findings highlight the efficacy of wavelet-based processing in enhancing the diagnostic resolution of GPR surveys, thereby enabling more effective non-destructive evaluation of large hydraulic structures. Traditional frequency or time-domain analyses often struggle to differentiate between air cavities and solid inclusions, such as boulders, in masonry structures, since both exhibit similar hyperbolic features in the radargram. By contrast, the CWT–TEDA framework enables a more precise separation of relevant signals from background interference, allowing characterisation based on the decay coefficient value. Experimental observations further indicate that the application of gain influences the amplitude enhancement of reflected signals but does not alter the inherent decay trend associated with subsurface features. While gain improves signal visibility and interpretability, the relative behaviour of the time-energy decay coefficient remains consistent, confirming that the decay-based interpretation is governed by material characteristics rather than amplitude scaling. In contrast, without gain, deeper reflections exhibit reduced clarity due to natural attenuation, which may obscure subtle anomalies despite the persistence of the same decay behaviour. In this regard, the study provides an incremental scientific advance by validating the usefulness of a decay coefficient-based interpretation for condition assessment of complex masonry systems.

Observations from the controlled model structure show that detection performance is influenced by the depth at which air cavities are located and their thickness. A 750 MHz GPR antenna with depth resolution of 1–3 m was found effective in detecting air cavities in the controlled model structure, and cavities with thicknesses less than the wavelength of the electromagnetic wave were undetected by the method. Also, anomaly ID A10 in Table 2 was not detected by the

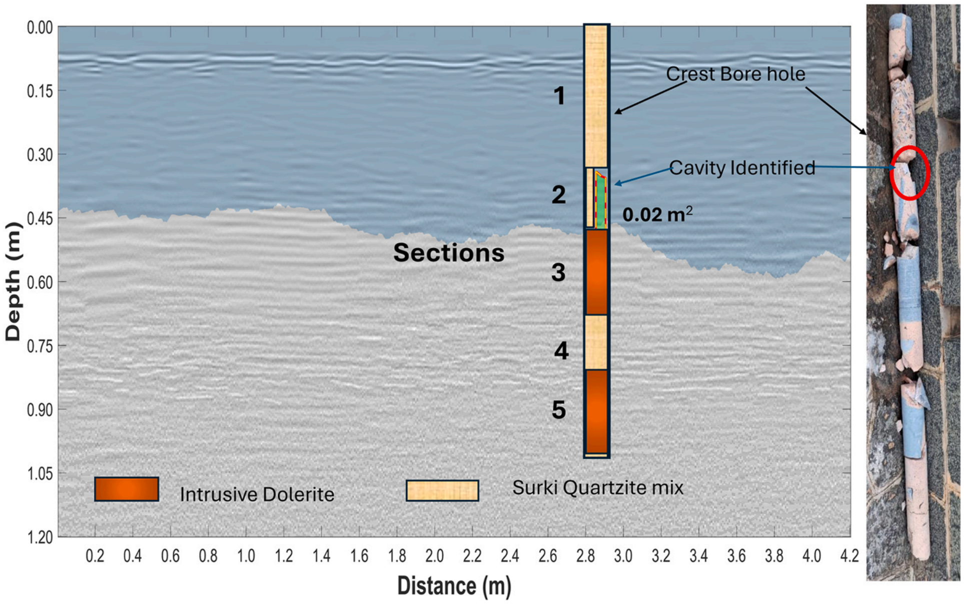

Fig. 15. B-Scan image overlaid by anomaly regions annotated with the area of anomalous sections for the dam crest.

method using a 750 MHz GPR antenna with a wavelength of 16 cm in a masonry structure, with the original thickness of the air cavity being 10 cm. Detected cavities in the model structure showed slight variation from the field condition, with a percentage error less than 15%, which was due to wave-penetration characteristics. Air cavities whose thickness is significantly smaller than the electromagnetic wavelength are difficult to resolve due to insufficient phase separation of reflected waves, while cavities satisfying integer multiples of half-wavelengths exhibit stable interference patterns that enhance detectability; excessively large cavities, however, may introduce complex internal reflections that reduce diagnostic contrast. GPR survey of the model structure, with packed and unpacked air-cavity regions underneath, clearly reveals the decay coefficient characteristics of air cavities and solid inclusions.

Even though the 750 MHz antenna shows good depth resolution for 1–3 m, in a field study on the dam spillway and crest with stone masonry and lime-surki mortar, the 450 MHz antenna has effectively identified the air cavities, with a percentage error of 6% in the 1–3 m depth range. These findings reveal that cavity detectability is governed by the relationship between cavity thickness and the electromagnetic wavelength, thereby emphasising the critical role of careful GPR antenna selection in reliable subsurface characterisation. MASW survey and core drilling in the dam sections further validated the results.

4.5. Limitations and future scope

The results indicate a practical limitation in cavity detectability, which depends strongly on how their thickness compares with the electromagnetic wavelength used in the survey. When cavity dimensions are not well matched to the operating wavelength, the resulting wave interference can be weak or unstable, leading to ambiguous responses. This emphasises the need for careful selection of GPR antenna frequencies to ensure reliable interpretation. Detection capability is further affected by cavity depth, material heterogeneity, and wave penetration behaviour, all of which can introduce additional uncertainty under real field conditions. In addition, elevated later-time energy in real GPR data may arise from multiple non-unique factors, including strong deep reflectors, constructive wave interference, variations in moisture or dielectric properties, and acquisition or processing effects, further complicating interpretation. Accordingly, the decay coefficient (α) is not intended as a standalone or universal discriminator, but rather as a context-dependent diagnostic indicator evaluated within the controlled conditions of this study.

Future work will aim to address these challenges by employing multi-frequency and multi-polarisation GPR measurements, which can provide broader wavelength coverage and improve sensitivity to cavities of different sizes. The present work focuses on the characterisation of air-filled cavities and solid inclusions, such as boulders, during the dry season with low water levels in dams. The proposed framework will also be extended to water-filled cavities and full-reservoir conditions, where changes in dielectric properties and boundary effects are expected to alter wave interference and energy-decay characteristics. In addition, combining the method with numerical modelling and machine learning–based classification is expected to further enhance anomaly characterisation and support more efficient large-scale assessments.

5. Conclusion

This study highlights the critical role of geophysical methods in enhancing the monitoring and maintenance of various masonry dam sections, including the spillway and crest. A new, stable method for higher-order processing of GPR data is proposed to improve the detection and delineation of subsurface anomalies in masonry dam structures. By overcoming the inherent shortcomings of traditional GPR B-scan interpretations, the new method uses the Continuous Wavelet Transform and Time-Energy Density Analysis to provide higher-resolution quantitative information on subsurface conditions. This integration enables effective time-frequency localisation of non-stationary GPR signals, and TEDA facilitates the extraction of meaningful energy-decay patterns that reveal subsurface material properties. One of the most important results of this analysis is the differentiation between air cavities and boulder features that classically give rise to identical hyperbolic reflections on radargrams by interpreting energy-decay coefficients. Negative decay coefficients indicate air voids, whereas positive values indicate denser materials such as boulders or solid mortar. Such a differentiation enables more accurate identification and classification of subsurface features and reduces the chances of misinterpretation. The practical implementation of this technique was established on a controlled masonry model and various sections of actual dam structures. Field measurements consistently confirmed the presence of critical subsurface flaws, including air pockets and heterogeneous material content. These observations were independently cross-validated by other methods, such as MASW surveys and borehole coring, thus substantiating the validity and diagnostic precision of the TEDA-CWT technique.

Additionally, this technique allows for the spatial quantification of anomalies in a manner that cannot be achieved with conventional GPR B-scans. The ability to define the extent and depth of deteriorated or weakened areas enables more accurate planning of remedial work, such as grouting, making the process more efficient and cost-effective. The observed correlation between decay behaviour and subsurface heterogeneity provides a new interpretative framework grounded in signal physics, further enriching non-destructive geophysical assessments. Together, these efforts highlight the potential of integrating advanced signal-processing techniques with geophysical surveying as a robust and physically informed approach for non-destructive evaluation, ultimately contributing to the long-term safety and sustainability of masonry dam infrastructure. However, cavity detectability is constrained by the relationship between cavity dimensions and the electromagnetic wavelength, with depth and material heterogeneity further introducing uncertainty under field conditions. These findings highlight the importance of careful selection of GPR antenna frequency to ensure reliable and stable interpretation. Future work will address these limitations through multi-frequency and multi-polarisation surveys and by extending the framework to water-filled cavities and full-reservoir conditions, thereby improving robustness for long-term assessment of masonry dam infrastructure. In addition to that, numerical modelling can be used to improve physics-based interpretation of wave–structure interactions, alongside machine learning–based classification to enable efficient and automated large-scale assessment.

CRediT authorship contribution statement

K Panjami: Writing – review & editing, Writing – original draft, Software, Methodology, Investigation, Formal analysis, Data curation, Conceptualization. **Panjamani Anbazhagan:** Writing – review & editing, Supervision, Resources, Funding acquisition, Conceptualization.

Declaration of Competing Interest

The authors declare the following financial interests/personal relationships which may be considered as potential competing interests: P Anbazhagan reports financial support was provided by Central Water Commission. If there are other authors, they declare that they have no known competing financial interests or personal relationships that could have appeared to influence the work reported in this paper.

Acknowledgment

The authors gratefully acknowledge the contributions of Mr Chandan Gowda and Mr Yogarish Raja for their invaluable assistance in field testing. The authors would like to thank the Dam Safety (Rehabilitation)

Directorate, Central Water Commission (CWC) for funding the “International Centre of Excellence in Dam Engineering” (ICED) under the Dam Rehabilitation and Improvement Project (DRIP); Ministry of Jal Shakti (MoJS), Government of India for the project entitled “Integrated Investigation for Risk Assessment of the Dam” under grant R-24011/57/2023-Pen Riv Section-MOWR.

Data availability

Data will be made available on request.

References

[1] Gholamhossein Akbari, Dam instability risk analysis of damaged spillway, Eng. J. 17 (4) (2013) 1–8, https://doi.org/10.4186/ej.2013.17.4.1.

[2] Fiedler, Managing dam safety risks related to hydraulic structures managing dam safety risks related to hydraulic structures, 6th Int. Symp Hydraul. Struct. Hydraul. Struct. Water Syst. Manag. (2016), https://doi.org/10.15142/T3720628160853.

[3] Pavel Novák, A.I.B. Moffat, Chandra Nalluri, R.A.I.B. Narayanan, Hydraulic Structures, CRC Press, 2017.

[4] Guochen Zhang, Liqun Xu, Fei Qiu, Zhiyuan Shen, Yin Zhang, A review on the progress of integrated geophysical exploration techniques for leakage hazard detection in earth and rock dams, Appl. Sci. 15 (4) (2025) 1767, https://doi.org/10.3390/app15041767.

[5] W.F. Kepler, L.J. Bond, D.M. Frangopol, Improved assessment of mass concrete dams using acoustic travel time tomography. Part II—application, Apr 12, Constr. Build. Mater. 14 (3) (2000) 147–156.

[6] V. Karastathis, P. Karmis, Investigation of seepage and settlement problems at the Mornos earth dam, Greece, by geophysical methods, May 11. Symposium on the Application of Geophysics to Engineering and Environmental Problems, GeoScienceWorld, 2012 (pp. 180-180).

[7] Federico Lombardi, Maurizio Lualdi, Elsa Garavaglia, Masonry texture reconstruction for building seismic assessment: practical evaluation and potentials of ground penetrating radar methodology, Constr. Build. Mater. 299 (September) (2021) 124189, https://doi.org/10.1016/j.conbuildmat.2021.124189.

[8] Xin Sui, Zhen Leng, Siqi Wang, Xing Cai, Minghui Gong, Lei Zhang, In-situ grouting rate prediction of semi-flexible pavement based on a novel composite dielectric constant model and ground-penetrating radar, Constr. Build. Mater. 438 (August) (2024) 137209, https://doi.org/10.1016/j.conbuildmat.2024.137209.

[9] Leonard J. Bonda, William F. Kepler, Dan M. Frangopol, Improved assessment of mass concrete dams using acoustic travel time tomography. Part II-application, Constr. Build. Mater. 14 (2000) 147–156.

[10] T. Gołębiowski, B. Piwakowski, M. Ćwiklik, A. Bojarski, Application of combined geophysical methods for the examination of a water dam subsoil, Oct 22, Water 13 (21) (2021) 2981.

[11] D.P. Bigman, D.J. Day, Ground penetrating radar inspection of a large concrete spillway: A case-study using SFCW GPR at a hydroelectric dam, Jun 1, Case Stud. Constr. Mater. 16 (2022) e00975.

[12] Xiulin Li, Lifei Fan, Hao Huang, Jutao Hao, Meng Li, Application of ground penetrating radar in leakage detection of concrete face Rockfill Dam, IOP Conference Series Earth Environmental Science 189 (2018), https://doi.org/10.1088/1755-1315/189/2/022044.

[13] J.M. Glover, "Void detection using standing wave analysis, Pap. Geol. Soc. Can. 1992 (1992) 63–73.

[14] Lev Kofman, Amit Ronen, Sam Frydman, "Detection of model voids by identifying reverberation phenomena in GPR records, J. Appl. Geophys. 59 (4) (2006) 284–299.

[15] L. Kofman, "Use of ground penetrating radar in geotechnical applications, Proc. 12th Conf. Isr. Assoc. Adv. Miner. Eng. Eilat (1994).

[16] L. Kofman, "Use of georadar for detection of underground structural irregularities. ANNUAL MEETING-ISRAEL GEOLOGICAL SOCIETY, LASER PAGES PUBLISHING, LTD., 1996.

[17] Yaacov Arkin, A. Gilat, Lev Kofman, "Developing Dead Sea sinkholes revealed by ground penetrating radar, Geol. Surv. Isr. Curr. Res. 12 (2000) 25–30.

[18] Qiuqin Yu, et al., "Cement pavement void detection algorithm based on GPR signal and continuous wavelet transform method, Sci. Rep. 13 (1) (2023) 19710.

[19] Xingxin Xu, Qiaosong Zeng, Dong Li, Jin Wua, Xiangan Wu, Jinyin Shen, GPR detection of several common subsurface voids inside dikes and Dams, Eng. Geol. 111 (2010) 31–42.

[20] Regidestyoko Wasistha Harseno, Sung-Jin Lee, Seong-Hoon Kee, Sungmo Kim, Evaluation of air-cavities behind concrete tunnel linings using GPR measurements, Remote Sens. 14 (October) (2022) 5348, https://doi.org/10.3390/rs14215348.

[21] Armand Abordán, Norbert Péter Szabó, 2021, Machine Learning Based Approach for the Interpretation of Engineering Geophysical Sounding Logs Acta Geodaetica Et Geophysica.” https://link.springer.com/article/10.1007/s40328-021-00354-4?utm_source=chatgpt.com.

[22] Liang Zhang, Tonghua Ling, Bin Yu, Fu Huang, Sheng Zhang, Intensive interferences processing for GPR signal based on the wavelet transform and f-k filtering, J. Appl. Geophys. (2021). ⟨https://www.elsevier.com/locate/jappgeo⟩.

[23] R. Hussein, B. Etete, H. Mahdi, H. Al-Shukri, “Detection and delineation of cracks and voids in concrete structures using the ground penetrating radar technique”, J. Appl. Geophys. 226 (2024) 105379.

[24] L. Jiao, Q. Ye, X. Cao, D. Huston, T. Xia, Identifying concrete structure defects in GPR image, Measurement 160 (2020) 107839.

[25] Tonghua Ling, Wenchao He, Sheng Zhang, Xianjun Liu, Fu Huang, Wenjun Liu, A new method for measuring the relative dielectric constant of porous mixed media using GPR, and its application, Constr. Build. Mater. 353 (October) (2022) 129042, https://doi.org/10.1016/j.conbuildmat.2022.129042.

[26] S.G. Mallat, A Theory for Multiresolution Signal Decomposition: The Wavelet Representation, in: IEEE Transactions on Pattern Analysis and Machine Intelligence, 11, IEEE, 1989.

[27] Ingrid Daubechies, Wim Sweldens, Factoring Wavelet Transforms into Lifting Steps, in: Journal of Fourier Analysis and Applications, 4, Lecture Notes in Earth Sciences, 1998.

[28] Yves Meyer, Wavelets and Operators, Cambridge University Press, 1990.

[29] David J. Daniels, Ground Penetrating Radar 1 (2004) (Iet).

[30] A.P. Annan, Electromagnetic principles of ground penetrating radar, Ground penetrating radar theory appl. (2009) 1–40.

[31] K. Meyer, E. Erdogmus, G. Morcous, M. Naughtin, Use of ground penetrating radar for accurate concrete thickness measurements, AEI 2008 Build. Integr. Solut. (2008) 1–10.

[32] Constantine A. Balanis, Balanis' Advanced Engineering Electromagnetics, John Wiley & Sons, Hoboken, NJ, USA, 2024.

[33] Choon B. Park, Richard D. Miller, Jianghai Xia, Multichannel analysis of surface waves, Geophysics 64 (3) (1999) 800–808.

[34] Koya Suto, An application of multichannel analysis of surface waves (MASW) to hydrological study: a case history, ASEG Ext. Abstr. 2012 (2012) 1–4, https://doi.org/10.1071/ASEG2012ab044.